Biaxial tearing properties of woven coated fabrics using digital image correlation

Rijin He [a], Xiaoying Sun [a, b,*], Yue Wu [a, b], Guowen Tang [c], Valter Carvelli [d]

[a] *Key Lab of Structures Dynamic Behavior and Control of the Ministry of Education, Harbin Institute of Technology, Harbin 150090, China*

[b] *Key Lab of Smart Prevention and Mitigation of Civil Engineering Disasters of the Ministry of Industry and Information Technology, Harbin Institute of Technology, Harbin 150090, China*

[c] *China Railway First Survey and Design Institute Group Co., Ltd., Xi'an 710000, China*

[d] *Department of Architecture, Built Environment and Construction Engineering, Politecnico di Milano, Milan, Italy*

[*] *Corresponding author. E-mail address: sxy_hit@163.com*

Abstract: Architectural fabrics as construction materials can experience tearing failure caused by inevitable flaws, which greatly degrade the tensile resistance. This paper presents an experimental study which deals with the crack tearing properties of PVC coated fabrics. Effect of the initial crack length and orientation on tearing behavior were investigated with quasi-static biaxial tensile loading of cruciform specimens, setting the same load rate in warp and weft directions. The brittle failure of the PVC coated fabric had always the crack propagation along warp or weft direction. Defining the tearing residual strength (TRS) as the residual load carrying capacity of a cracked fabric, it was found that the TRS decreased nonlinearly with the increase of initial crack length, but with negligible variation of the crack orientation. Moreover, to better

understand the tearing failure mechanism, the full field strain was measured by 2D Digital Image Correlation (DIC) technique. This provided a detailed distribution of the strain components near the crack tip during biaxial loading.

Keywords: coated fabric, biaxial loading, tearing properties, DIC

1. Introduction

Woven coated fabrics have been widely used in tension fabric structures, inflatable membrane structures and non-rigid airship structural envelopes for their high strength-weight ratio and good durability [1]. However, the existence of initial flaw from e.g. windborne debris can lead to severe stress concentration [2], which significantly deteriorate the load bearing capacity of the coated fabrics. Consequently, the tearing properties become one of the critical factors which affect the structural safety and the wide application of fabric structures.

In real applications, structural woven fabrics are usually under in-plane biaxial stress states along warp and weft directions, and the mechanical response is mainly dependent on the constituent materials properties as well as on the yarns interlacement, namely weaving pattern. Therefore, a realistic study on the mechanical properties of woven coated fabrics must consider biaxial tensile loading conditions and an accurate measurement of the deformation modes [1,3]. The deformation of woven coated fabric could be highly uneven, due to the intrinsic nature of the woven reinforcement. Traditional local contact instruments (e.g. strain gauges or LVDTs) cannot provide an accurate overview of the strain components distribution, in particular around a flaw zone as a crack. Thus, non-contact optical full-field techniques are preferable (sometimes

the only) for the measurement of the in-plane deformation of woven fabrics [4]. Therefore, biaxial tensile loading setup combined with full field strain measurement is particularly needed for a proper study of the tearing features of woven coated fabrics. This is one scope of the present study.

Central crack tearing studies of architectural fabrics and airship envelops have been extensively conducted by uniaxial tensile loading [2, 5-11], while studies involving biaxial tearing tests are still very limited. Szostkiewicz [12] and Bigaud [7] performed biaxial tearing test on PVC coated fabrics aiming to get the crack initiation stress. Besides, abrupt failure and progressive failure were firstly distinguished for different crack lengths, and an equivalent crack length was proposed to consider the combined effect of crack length and crack orientation. Godfrey [13] adopted initially slit cruciform specimens to investigate the biaxial tearing strength of seven kinds of military tent fabrics. A micromechanical model was proposed to predict the biaxial tearing strength. The adopted biaxial experimental setup can only apply a constant tension in one direction and an increasing tension in the other direction. Maekawa [8] conducted biaxial tearing tests on cruciform specimens of airship envelop to find out the relation between initial crack length and tear strength. Thiele's empirical formula and stress field model were used to predict the tear strength and to estimate the allowable slit size under the limit load condition. Luo [14] adopted a multi-axial testing device (four axis) to investigate the influences of the initial crack length and orientation on the mechanical performance of PVC coated fabric. The multi-axial tearing performances were similar to ones of biaxial tearing tests. Chen [15] and Wang [16] carried out comprehensive experimental biaxial tearing analyses of two kinds

of airship envelops including accurate observations of the tearing failure by a digital camera. Effect of initial crack length, crack orientation and biaxial stress ratio on tear strength were considered, and different tear strength models were compared.

In aforementioned studies, the main scope was the maximum tearing force or the tearing strength, with recordings of load-displacement curves and some observations of the tearing process. However, the strain field near the crack tip is of great importance to gain deep understanding of the tearing failure mechanism, but currently there is still lack of studies on the measurement of the full field strain at the crack tip.

Several researchers have adopted DIC technique as optical extensometer in uniaxial and biaxial tensile tests and picture frame shear tests of woven fabrics [17-22]. In the field of tension fabric structures, Dinh [23] exploited DIC technique to measure the full-field strain of an umbrella-shaped tension fabric membrane for foldable architectural applications under in-plane loading. Sun [24] employed stereovision technique to monitor the vibration of tensioned membrane structure in wind tunnel tests. These applications of DIC technique were for continuous tension fabric components without flaws. When defects (e.g. cracks) have to be considered, the tearing process creates large deformation and high strain gradients, hence particular attention must be dedicated to DIC measurements and calculations [25,26]. This is another scope of the present study.

Therefore, this paper presents an experimental study on the biaxial tearing properties of a PVC coated fabric with special attention paid to: the characterization of crack tip strain field exploiting DIC technique, the biaxial experimental setup, the data processing method for

parameter study and validation. Consequently, biaxial tearing properties of the woven coated fabric are detailed considering: tearing failure process, tearing residual strength (TRS) and crack tip strain field.

2. Material and Experimental methodology

2.1 Material and specimen

A typical architectural textile fabric was considered. It was a polyester yarn balanced plain weave fabric with polyvinylchloride (PVC) coating, manufactured by Hiraoka-Huifeng Membrane Co. Ltd. The weaving of polyester yarns of 1300 dtex created a fabrics of thickness 0.85 mm, and areal density 1100 g/m^2 after coating.

Cruciform specimen with arms aligned to the warp and weft directions was adopted for biaxial tearing test. The specimen dimensions are illustrated in Fig. 1 (a), the effective center part was 160×160 mm. To ensure proper transfer of the tensile load to the center part, three silts were cut in each loading arm, according to [27]. Each corner between two arms was smoothly transitioned with a circular arch to avoid stress concentration. Initial crack in the center of the specimen was introduced using #11 surgical blade, which allowed the cut of equal number of yarns per unit length. For the measurement of the full field strain by DIC technique, the center part of the specimen was randomly speckled with black permanent marker pen on the white coating surface of the fabric (see Fig. 1 (b)).

The effect of crack length and crack orientation on the tearing properties was studied by equi-biaxial loading in the warp and weft directions (load ratio 1:1). Different length and

orientation of the central crack were considered as summarized in the synopsis of the experimental program in Table. 1. Three specimens for each crack length and orientation were tested, and only one of them was adopted for the DIC analysis.

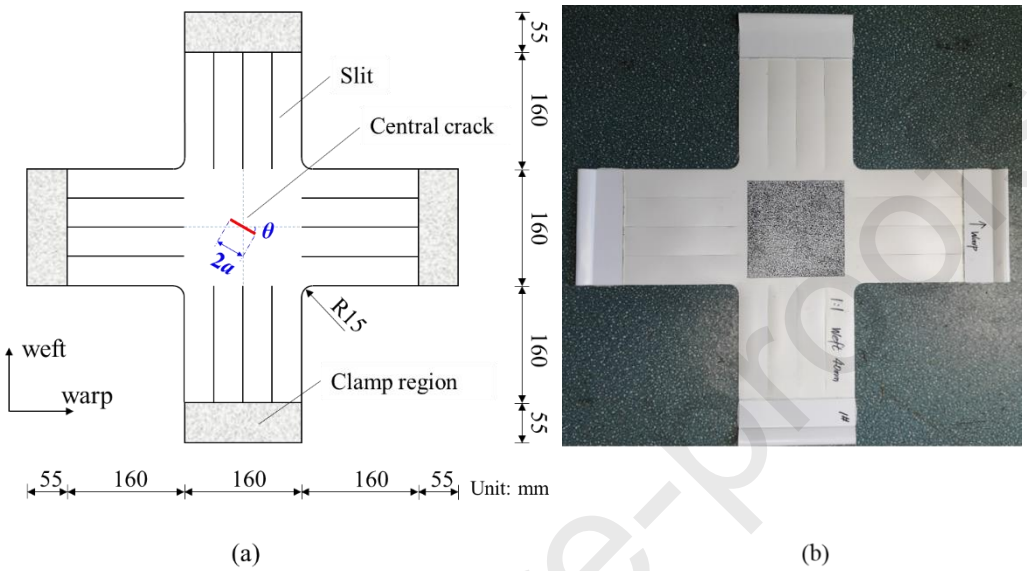

Fig. 1. Biaxial tearing specimen (a) dimension and (b) artificial speckle pattern for DIC.

Table. 1 Features of the experimental program

Load ratio	Crack length 2*a* (mm)	Crack orientation θ	Specimen number
1:1	10, 20, 40, 60, 80	0°/90°	30
	40	30°/45°/60°	9

2.2 Biaxial testing equipment

Biaxial tearing tests were conducted by a biaxial tensile machine developed by Space Structures Research Center at Shanghai Jiao Tong University (SJTU). This biaxial tensile apparatus is equipped with four independently controlled hydraulic servo actuator (see Fig. 2), which avoid the displacement of the specimen center during loading and hence undesired shear

strain components. Each actuator is equipped with a load cell of 30 kN and a clamp system.

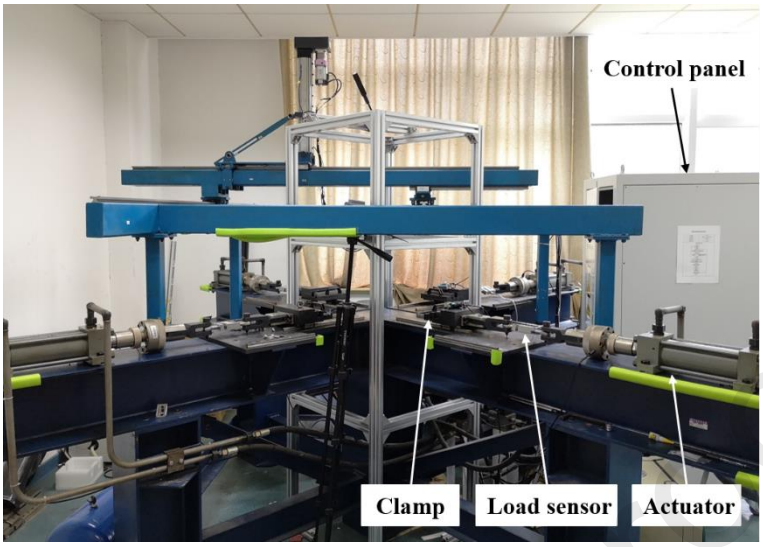

Fig. 2 Biaxial tensile machine in SJTU

The clamp system consists of a rubber pin inserted in the buttonhole of each arm and then clamped between two shaped metallic plates with screws as shown in Fig. 3 ([28,29]). Unlike traditional clamp systems which apply high pressure within the clamp region, the adopted allows free lateral contraction, reducing the stress concentration near the grips region which might lead to premature failure.

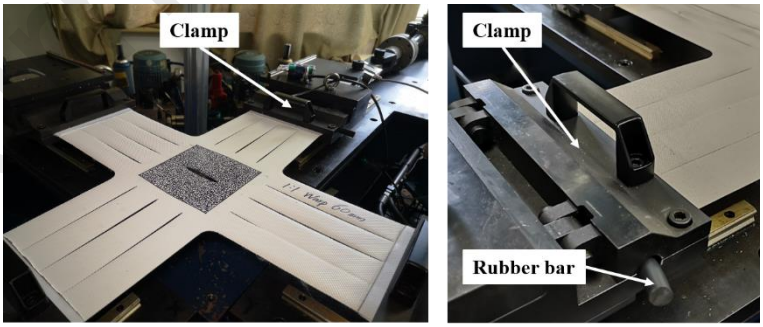

Fig. 3 Clamp system: (a) overview, and (b) detail of the rubber pin.

2.3 Digital Image Correlation (DIC) equipment and test setup

Assuming negligible out-of-plane deformation of the membrane specimen under in-plane biaxial tension, two-dimensional DIC technique was exploited. One digital camera was positioned perpendicular to the cruciform specimen (Fig. 4). The MER-1810-21U3C-L industrial digital camera produced by DAHENG IMAGING was used, with image sensor 1/2.3" Onsemi AR1820 rolling shutter CMOS, resolution of 4912×3864 pixels and pixel size of 1.25 μm. A Computar M0814-MP2 8mm F1.4 fixed lens was adopted. The working distance between the specimen surface and the camera was about 500 mm, which ensured fully cover of the center part of the cruciform specimen. The image acquisition frequency was set 1 Hz, because the loading rate was relatively slow. Before the beginning of the tearing test, camera calibration procedure was conducted using a 2D planner checkerboard. It consisted of 12×9 black and white squares (grid size 5 mm × 5 mm). At least 9 images of the checkerboard in different positions were captured and processed by the Camera Calibration Toolbox in MATLAB.

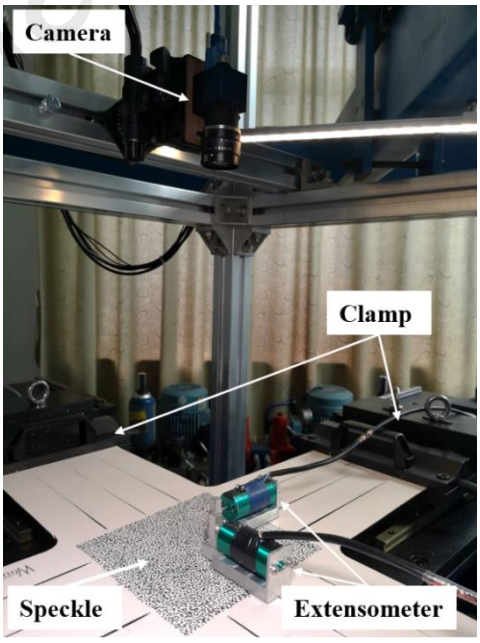

Fig. 4 Experimental set up of DIC

2.4 Experimental procedure

To ensure correct planarity of the specimen, a pre-tension load of 200 N was applied on each arm before starting the tearing test. Then, the calibration procedure of DIC was conducted on the initial stress state. Afterwards, monotonous loading was applied on each arm until completely tearing failure. Note that, the DIC images acquisition and the loading program were triggered simultaneously for a proper synchronization of load and image. Unlike commonly used biaxial displacement-controlled loading protocol, the adopted biaxial tensile machine had force controlled loading which ensured the imposed stress ratio. To avoid dynamic effects, a relatively slow loading rate 4 kN/m/min was employed. The data sampling frequency of the actuator displacement and load cell was 10 Hz, while the images sampling frequency was 1 Hz.

3. Preliminary DIC parametric studies

When adopting DIC technique to capture the full field strain during the tearing process, no default values are suggested for DIC parameters due to the discontinuous displacement filed, large deformation and significant stress concentration. Therefore, a parametric study was conducted to select proper DIC parameters.

3.1 Background on digital image correlation technique

The core idea of DIC technique is to evaluate the full field displacements through a series of digital images taken from the surface of test sample. Firstly, the intensity value matrix of digital images is discretized into small subsets, and then the image correlation algorithm solves

an optimization problem to match each small subset of the current reference image to the corresponding subset in the next deformed image. During the subset matching process, the subset is moved by a step size of *n* pixels to search the corresponding subset after deformation, *n* must be smaller than the subset size to enable overlapping of the subset [32]. Once the displacement field is obtained, the strain field can be subsequently estimated through differentiation of the displacement field. The resolution of the strain field depends on the strain window size used in the differentiation algorithm. A proper strain window size is also a compromise of spatial resolution and noise reduction.

The DIC analyses were performed by the open source 2D DIC software Ncorr v1.2 [30]. It employs two different image correlation algorithms to find the deformation of each subset. The Zero-mean Normalized Cross-Correlation (ZNCC) function is used to obtain the initial guess as shown in Eq. (1), which indicates a good match when C_{ZNCC} approaches 1. The Zero-mean Normalized Sum of Square Difference (ZNSSD) function is also used to refine the initial guess with sub-pixel resolution as shown in Eq. (2). C_{ZNSSD} approaching 0 indicates a good match. Further examples on application of Eqns. (1, 2) in DIC analysis can be found in [31].

$$C_{ZNCC} = \frac{\sum_{(i,j)\in S}\left[f(x_i^{ref}, y_j^{ref}) - f_m \right] \times \left[g(x_i^{cur}, y_j^{cur}) - g_m \right]}{\sqrt{\sum_{(i,j)\in S}\left[f(x_i^{ref}, y_j^{ref}) - f_m \right]^2 \times \sum_{(i,j)\in S}\left[g(x_i^{cur}, y_j^{cur}) - g_m \right]^2}} \tag{1}$$

$$C_{ZNSSD} = \sum_{(i,j)\in S}\left[\frac{f(x_i^{ref}, y_j^{ref}) - f_m}{\sqrt{\sum_{(i,j)\in S}\left[f(x_i^{ref}, y_j^{ref}) - f_m \right]^2}} - \frac{g(x_i^{cur}, y_j^{cur}) - g_m}{\sqrt{\sum_{(i,j)\in S}\left[g(x_i^{cur}, y_j^{cur}) - g_m \right]^2}} \right]^2 \tag{2}$$

where $f(x_i, y_j)$ and $g(x_i, y_j)$ are the image grayscale intensity functions of the reference image and current image at point (x_i, y_j) in subset *S*. f_m and g_m are the mean grayscale values of the

reference and current subset.

To cope with the discontinuous displacement field, such as the crack opening and propagation, DIC analysis was performed on the current configuration, since the discontinuities are easier to distinguish. After that, a dedicated Euler-Lagrange algorithm was adopted to convert the displacement to the reference configuration. To prevent possible distortions in the displacement field near the highly nonlinear crack tip region, the subset truncation was enabled.

3.2 Parametric studies

There are three adjustable parameters in DIC analysis, namely: subset size, subset spacing and strain window size [32,33]. The subset size and spacing can significantly affect the computation time and accuracy, the strain window size does not affect the computation time but can affect the spatial resolution of strain field. Thus, a set of parametric studies were conducted to optimize these parameters.

The tearing test with initial crack 20 mm along the weft direction (90°) was selected for the parametric studies. Since the attention was mainly focused on the strain field near the crack, a reduced region of interest (ROI) was adopted to save computation time, as shown in Fig. 5. The size of ROI was 130 mm and 60 mm along and perpendicular to the crack direction, respectively. Due to the development of large strain around the crack, Eulerian-Almansi strain tensor was considered and adopted in the following. The strain component ε_{yy} on the y=0 line was extracted to investigate the effect of subset size, subset spacing and strain window size.

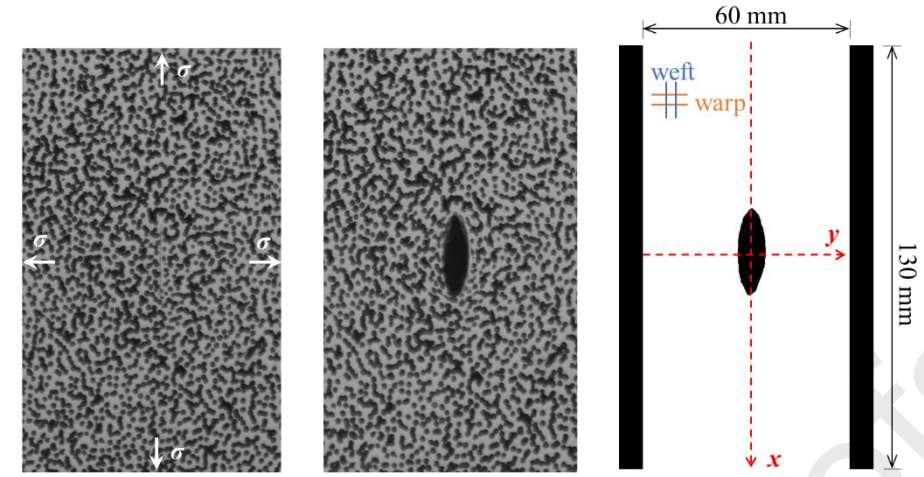

Fig. 5 (a) Reference configuration, (b) current configuration and (c) ROI

3.2.1 Effect of subset size

For a given ROI, the larger the subset, the more grayscale and featured information it contains. Therefore, it is easier to distinguish it from other subsets, consequently the matching accuracy is higher. On one hand, the number of pixels in the subset is larger, thus it takes more computation time. But on the other hand, the larger the subset is, the fewer subsets the ROI contains, which result in lower spatial resolution. Thus, a suitable subset size is a compromise of accuracy, resolution and computation time [32].

To investigate the effect of subset size, DIC analysis was conducted with fixed subset spacing of 2 pixels and strain window size of 5 pixels, while the subset size ranging from 10 to 40 pixels. The strain component ε_{yy} on the line y=0 is shown in Fig. 6. It can be seen that with the increase of subset size, the strain field become smoother and can better represent the peak point of the strain. For the subset size of 10 pixels, the strain distribution was affected by considerable noise and cannot be acceptable. For subset size larger than 20 pixels, the strain

field showed the same distribution except for the peak value. However, the computation time of larger subset size is usually several time higher than that of small one. As a compromise of accuracy and computation time, the subset size of 30 pixels was adopted in this study.

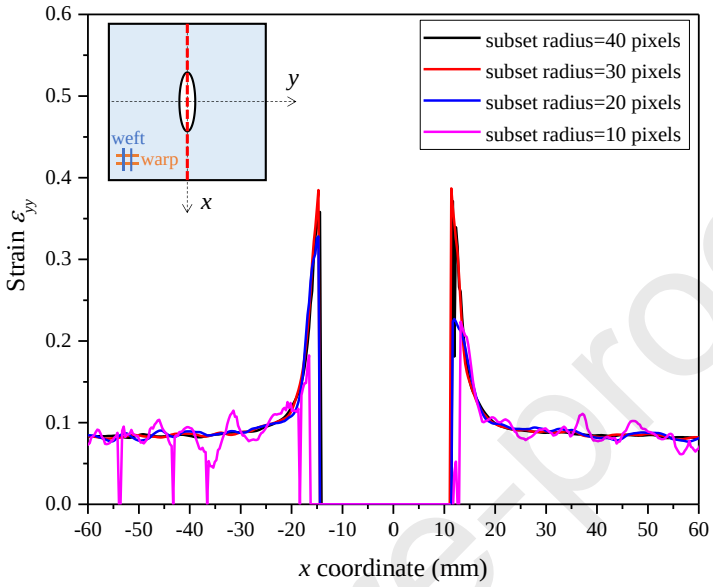

Fig. 6 Strain ε_{yy} on the line y=0 with different subset size

3.2.2 Effect of subset spacing

The subset spacing controls the density of DIC data points and influences the spatial resolution. Larger subset spacing can reduce the computation time greatly but meanwhile decreases the spatial resolution to some extent. Generally, it is recommended to choose a subset spacing of 1/3 to 1/2 of the subset size so that neighboring subsets partially overlap [32]. However, if the gradient of the Quantity-of-Interest (QOI) is relatively large, such as strain concentration near the crack tip, small subset spacing is needed to capture the peak point of the QOI.

To investigate the effect of subset spacing, DIC analysis was conducted with fixed subset size of 30 pixels and strain window size of 5 pixels, while the subset spacing ranging from 1

pixel to 6 pixels. The strain component ε_{yy} on the line y=0 is shown in Fig. 7. The larger is subset spacing, the smoother is the strain field, with significantly lower spatial resolution. For subset spacing equals to 1 pixels, the strain field shows obviously fluctuation due to the effect of noise. For subset spacing equals to 6 pixels, the strain field shows lower spatial resolution due to lack of data points. Generally, smaller subset spacing also need higher computational cost than that of larger ones. Thus, as a compromise, the subset spacing of 4 pixels was adopted.

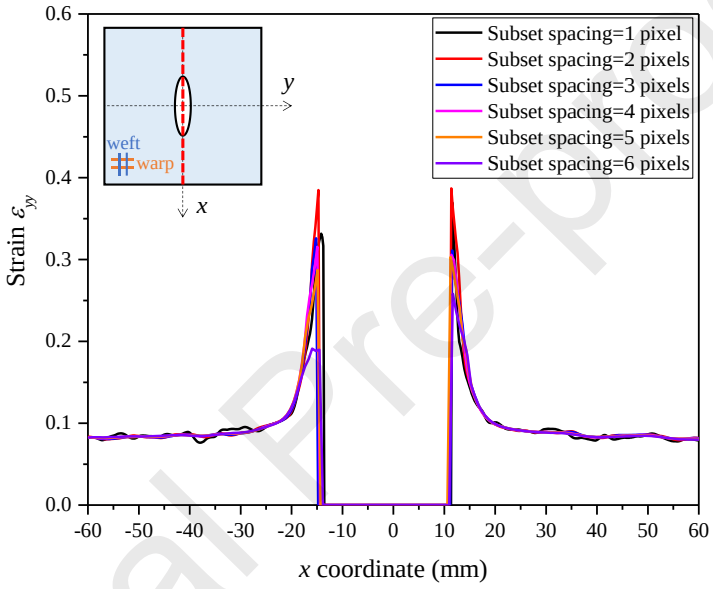

Fig. 7 Strain ε_{yy} on the line y=0 with different subset spacing

3.2.3 Effect of strain window size

The strain field is computed by differentiating the displacement field. To avoid possible noise by differentiating the displacement at discrete locations, 2D polynomial function is adopted to fit the local region of displacement field [34]. Such analytical expression is then used to calculate the strain components. The local region of the displacement data adopted in the least square plane fitting is named the strain window. A valid strain window size should be small enough to get the best displacement approximation, but not so small to avoid noisy of the

strain, especially in the high deformation gradient regions.

From the Ncorr GUI, the plane fitting result can be visualized in real time at any point. It was found that a strain window size of 5 pixels can give the best displacement field fitting. As shown in Fig. 8 and Fig. 9, smaller strain window size would cause significant noise, larger strain window size would cause over-smoothing problem which reduce the resolution.

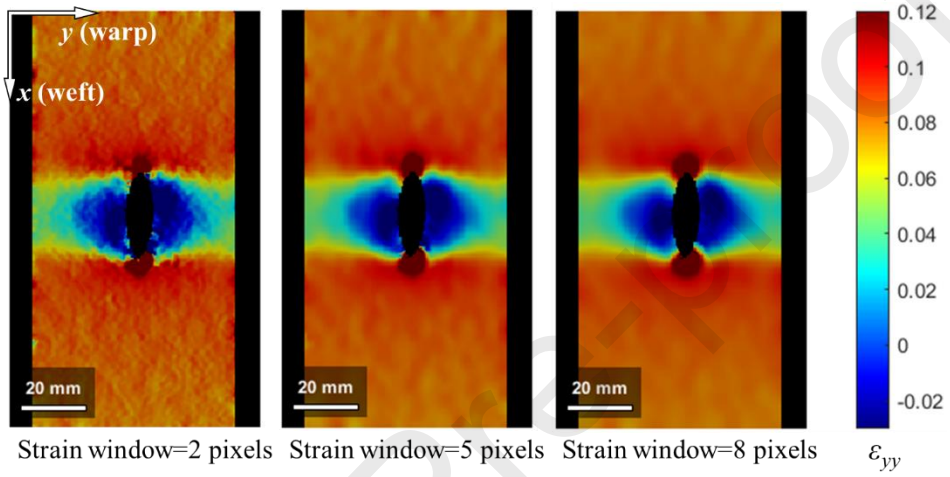

Fig. 8 Strain ε_{yy} maps obtained from different strain window size

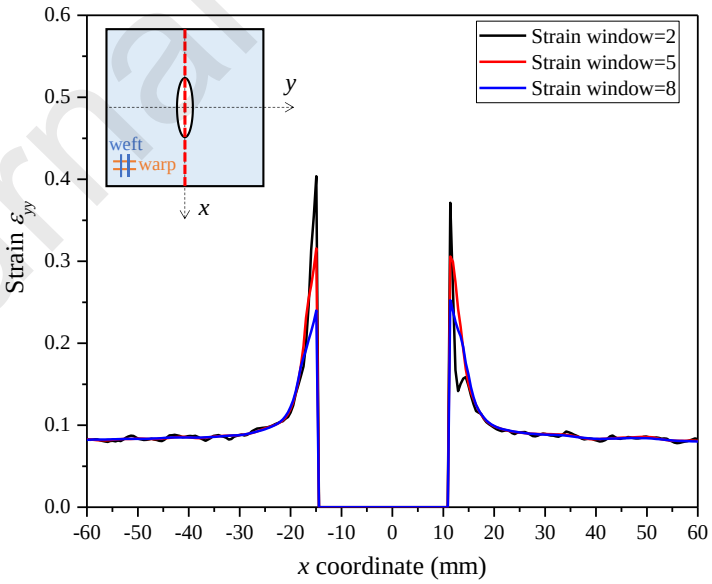

Fig. 9 Strain ε_{yy} on the line y=0 with different strain window size

3.2.4 Comparison of the DIC and extensometer measurements

According to the above parametric study, the optimized DIC parameters for further analyses are: subset size 30 pixels, subset spacing 4 pixels, strain window size 5 pixels. These parameters can provide a smooth strain field and relatively high spatial resolution. It should be highlighted that the maximum strain at crack tip is a 'point' value and it can be affected by many factors, such as material defects, experimental error, noise, and most importantly DIC parameters. Thus, the size of strain concentration zone may be more meaningful than the exact value of the maximum strain.

In order to verify the accuracy of the DIC technique, a biaxial cycling tensile test was also conducted in which two needle extensometers (LP-20F, Midori, Japan) were installed to measure the local strain, as shown in Fig. 4. Their gage length was 40 mm and accuracy 0.2 mm. The cycling loading spectrum is shown in Fig. 10 (a), the corresponding displacement of the first cycle is in Fig. 10 (b). The DIC data agree very well with the extensometer data, most of the error is below 5% which indicates that the DIC technique can provide reliable measurements. Moreover, the good accuracy of the DIC algorithm implemented in Ncorr was further verified by comparing to the software VIC-2D [35].

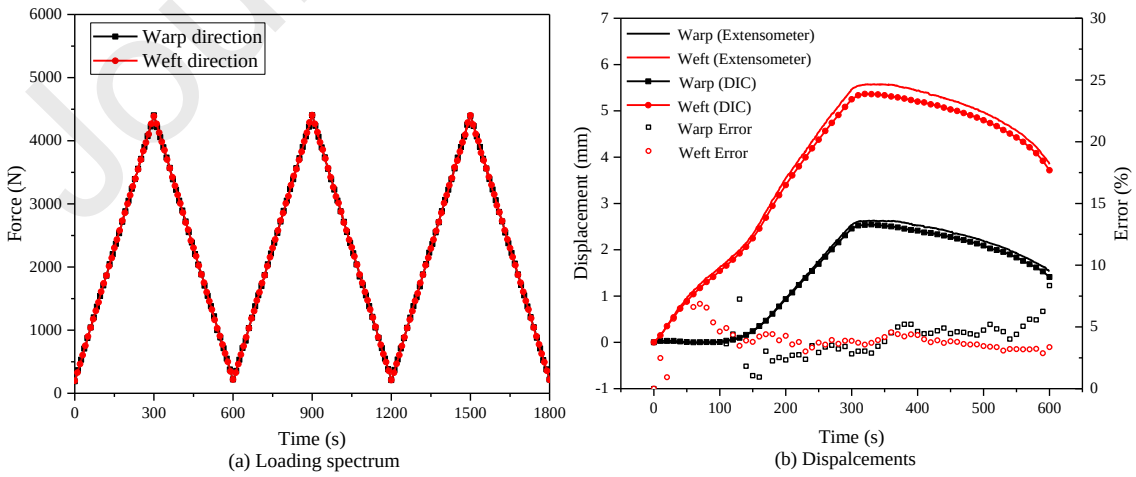

Fig. 10 Comparison of the displacement obtained by DIC and extensometer

4. Effect of initial crack length on biaxial tearing behaviors

Biaxial tearing properties under different initial crack lengths are analyzed, considering various features of the tearing response, namely: the tearing curves, the tearing residual strength, the tearing process and the strain fields.

4.1 Tearing stress-displacement curves

The biaxial tearing curves of different initial crack length are depicted in Fig. 11 and Fig. 12. The nominal stress is defined as $\sigma = F/160$, where F is the tensile load in corresponding arm, 160 refers to the arm width (unit: mm). Curves in warp and weft directions are significantly different. With the increase of initial crack length, it can be found that:

(i) Stiffness along the crack direction remains almost the same, curves in Fig. 11 (a) and Fig. 12 (b) almost overlap. However, the lower stiffness in the orthogonal to crack direction, as shown in Fig. 11 (b) and Fig. 12 (a), indicates considerable effect of the initial crack only on the mechanical properties in its perpendicular direction.

(ii) The peak value of nominal stress (also called tearing residual strength) has a nonlinear reduction with the crack length as shown in Fig. 13, see comments in section 4.2.

(iii) For all cases, tearing nominal stress decreases sharply after the peak value, which means a brittle failure. This is also connected to the force-controlled loading protocol. As the specimen's load carrying capacity decreases, the applied load still increases, so the failure is inevitably brittle.

(iv) In the direction perpendicular to the initial crack, the stress drops rapidly after the peak point, but not directly decreases to zero and can still increase at a low level, as shown in Fig. 11 (b) and Fig. 12 (a). This is because the applied load can reach a state of equilibrium with the adjacent loading arms after initial tearing failure [15]. Along the initial crack direction, there is no obvious stress drop as shown in Fig. 11 (a) and Fig. 12 (b). This is because the load carrying capacity in this direction is not affected by initial crack, but the biaxial tensile machine stopped loading after the abrupt increase in displacement due to the completely tearing failure.

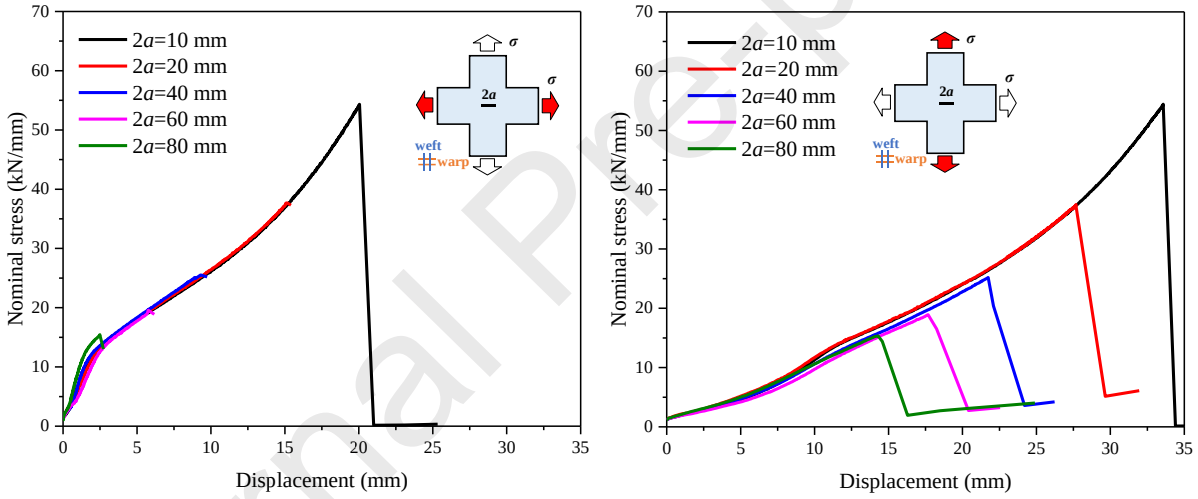

(a) Warp direction curves

(b) Weft direction curves

Fig. 11 Stress-displacement curves of specimens with different initial crack lengths (θ=0°, warp direction)

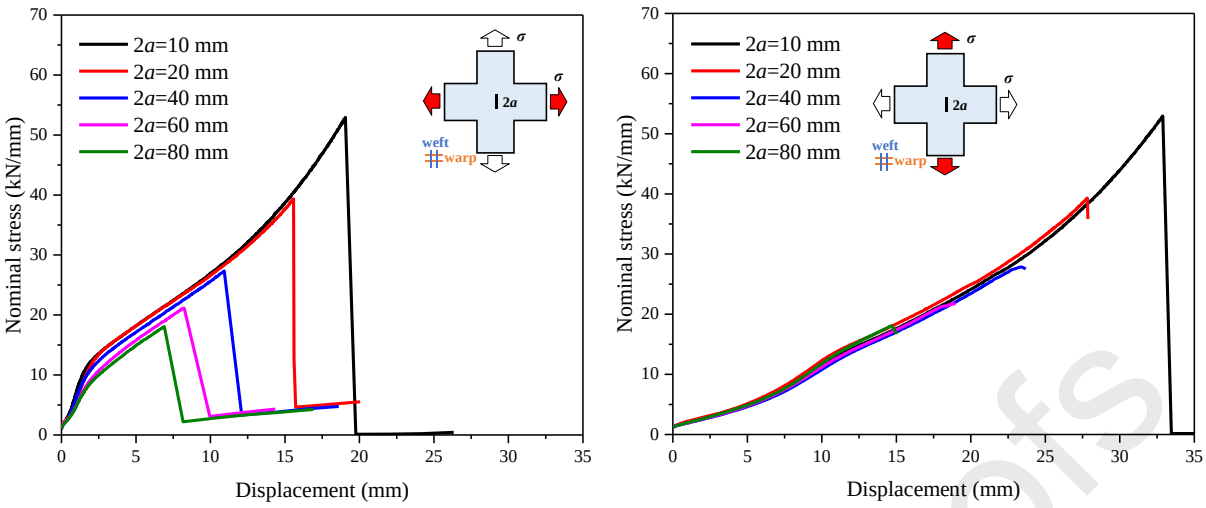

(a) Warp direction curves

(b) Weft direction curves

Fig. 12 Stress-displacement curves of specimens with different initial crack lengths (θ=90°, weft direction)

4.2 Tearing residual strength

Defining the tearing residual strength (TRS) σ_{res} as the maximum nominal stress depicted in Fig. 11 and Fig. 12, its mean values and standard deviations are illustrated in Fig. 13 and Table. 2. It can be clearly detected that the σ_{res} for warp crack and weft crack are very close to each other, this is because the balance architecture of the fabric. The nonlinear relationship between the tearing residual strength and the initial crack length can be well fitted by the empirical formulas in Eq. (3) and Eq. (4), both with coefficient of correlation R^2 higher than 0.996 which confirm the reliability of the fitting.

$$\sigma_{res}^{90} = 15.18 + 55.82e^{-0.0393 \cdot 2a} \tag{3}$$

$$\sigma_{res}^{0} = 14.78 + 56.95e^{-0.0425 \cdot 2a} \tag{4}$$

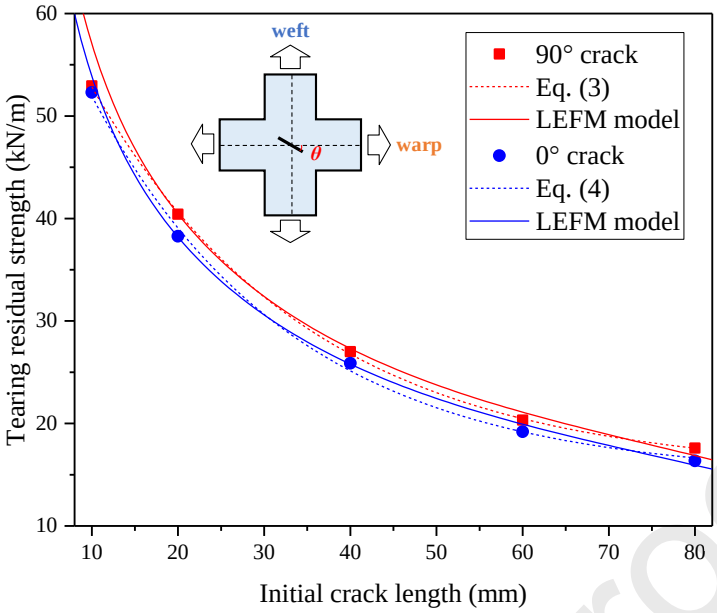

Fig. 13 Average tearing residual strengths under different initial crack length

Table. 2 Tearing residual strengths (average and standard deviation of three replicas) under different initial crack length (kN/m)

2*a* (mm)	Avg. TRS (*θ*=0°)	S.D.	Avg. TRS (*θ*=90°)	S.D.
10	52.30*	n.a.	52.94*	n.a.
20	38.26	1.27	40.41	1.51
40	25.87	0.63	27.01	0.38
60	19.20	0.39	20.33	1.23
80	16.36	0.79	17.60	0.67

* Specimens tend to break in the loading arm, only 1 out of 3 specimens had tearing failure.

According to linear elastic fracture mechanics (LEFM) theory, the fracture toughness can be calculated by [36]:

$$K_{IC} = F(a/W)\cdot\sigma_{res}\sqrt{\pi a} \tag{5}$$

Where $F(a/W)$ is the finite size correction factor. For the cruciform specimen in this study, $F(a/W)$ was estimated by finite element analyses (Appendix A), see e.g. [38-40]. Calculated $F(a/W)$ and K_{IC} are listed in Table 3.

The fracture toughness obtained by LEFM does not considerably vary with crack size (Table 3), except for $2a$=10mm where the small yielding assumption may not be satisfied. The averaged K_{IC} for $2a$ from 20mm to 80mm can be taken as material constants, that is, K_{IC}=204.65 kN·m$^{-1/2}$ for weft direction (θ=0°), K_{IC}=216.70 kN·m$^{-1/2}$ for warp direction (θ=90°). Thus, by substituting the constant K_{IC} into Eq. (5), the TRS can also be predicted as shown in Fig. 13.

Table. 3 Fracture toughness

$2a$ (mm)	$F(a/W)$ (-)	K_{IC} for θ=0° (kN·m$^{-1/2}$)	K_{IC} for θ=90° (kN·m$^{-1/2}$)
10	0.953	197.52	199.94
20	0.962	206.36	217.96
40	0.998	204.73	213.75
60	1.059	197.38	208.99
80	1.146	210.13	226.10
average	-	204.65	216.70

4.3 Tearing failure process and strain field analysis

Along with the acquisition of strain field by DIC technique, the tearing process can also be observed. Tearing failures are all brittle and without any yarn rupture before crack

propagation, the fracture paths follow the initial crack orientation, i.e. the crack propagation is self-similar. Considering the 90° crack (weft direction) with initial crack length of 40 mm as an example, the full-field strain as well as the tearing process is shown in Fig. 14. It can be seen that with the load increasing, the initial crack opens gradually and changes from sharp slit to spindle shape, the sharp crack tip becomes blunt. At the peak load, tearing failure occurs suddenly along the initial crack without any preliminary crack propagation.

The strain maps show uneven distribution in the vicinity of the crack. Far from the initial crack, the strain is quite uniform. The normal strain ε_{yy}, illustrated by Fig. 14 (a), had a circular concentration at each crack tip. The concentration zone as well as the average strain is getting larger with the increase of load. On the left and right side of the crack, there are two negative strain zones, which means the crack tends to close under biaxial loading due to the predominant Poisson's effect for the load along the crack (weft). The normal strain ε_{xx} illustrated by Fig. 14 (b), had a more uniform distribution than ε_{yy}, with a negative concentration at the crack tip which is consequence of the contraction in the weft direction (x) generated by the local peak of stress component in the warp one (y). The shear strain ε_{xy} illustrated by Fig. 14 (c), is negligible in most of the ROI, being the fabric loaded along its principal axes. Only at the crack tip, as expected, two symmetrical positive and negative shear strain zones are detected, which are related to the rotation of the material at the crack edge.

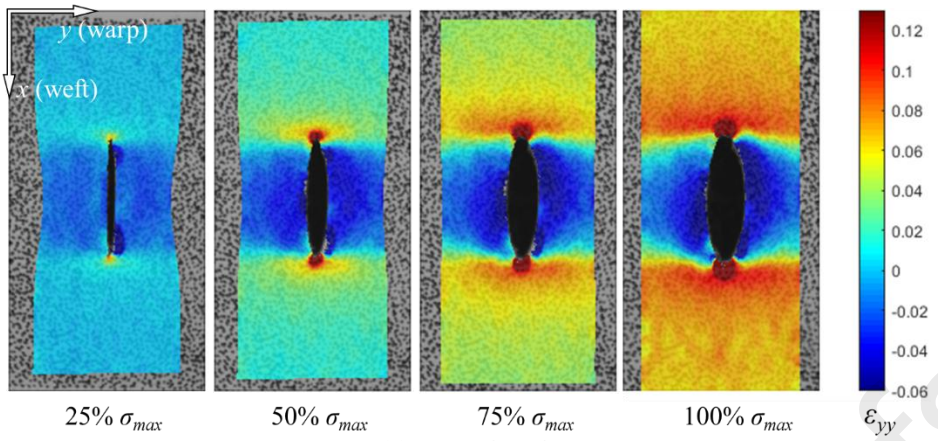

(a) Normal strain ε_{yy}

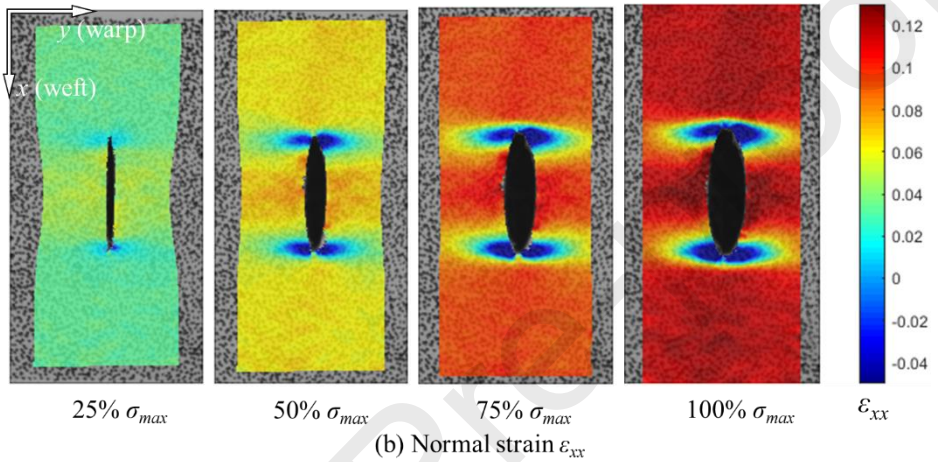

(b) Normal strain ε_{xx}

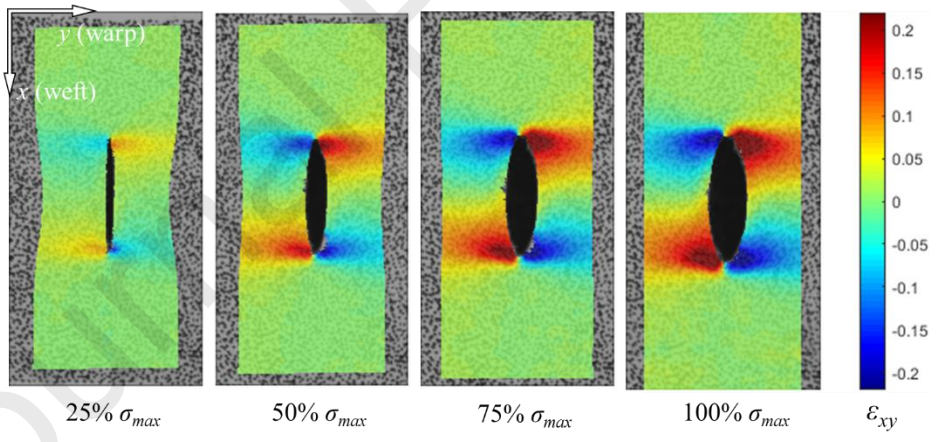

(c) Shear strain ε_{xy}

Fig. 14 Tearing morphology and full-field strain under different load level, (θ=90°, 2a=40 mm)

To better understand the evolution of strain concentration, the strain component ε_{yy} at different load levels along crack direction at y=0 is shown in Fig. 15, while ε_{yy} at 100% σ_{max} extracted along some paths perpendicular to crack direction is shown in Fig. 16.

Fig. 15 shows that with the increase of load level, both the average and the maximum strain increase. However, the strain ε_{yy} concentration is only limited in the vicinity of crack tip, about 5 mm, while is uniformly distributed away from the crack tip as shown in Fig. 16. At the load level of 25% σ_{max}, 50% σ_{max}, 75% σ_{max} and 100% σ_{max}, the average strain, which is calculated as the mean value of ε_{yy} on path A_4B_4 shown in Fig. 16, is 0.0011, 0.0149, 0.0405 and 0.0617 respectively, while the maximum strain is 0.0741, 0.2232, 0.3185 and 0.3424 respectively, thus the strain concentration factor, which is defined as the maximum strain divided by the average strain, decreases from 67.36 to 5.55. This is predictable by the Inglis's model [36], Eq. (6), which consider the initial crack as an elliptical hole of length 2a and half width b. The ratio of maximum and average stress (concentration factor) decreases with the increase of applied load, namely increase of b opening the crack.

$$\frac{\sigma_{\max}}{\bar{\sigma}} = 1 + \frac{2a}{b} \tag{6}$$

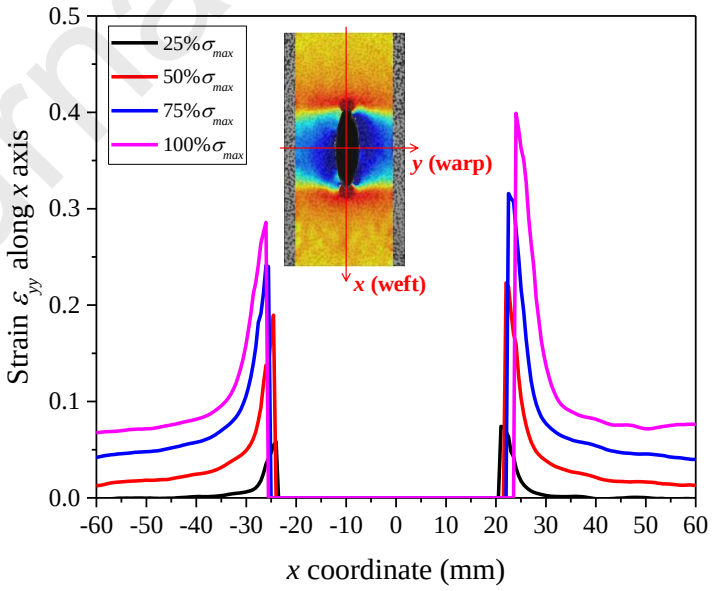

Fig. 15 Strain ε_{yy} on x axis, y=0 (θ=90°, 2a=40 mm)

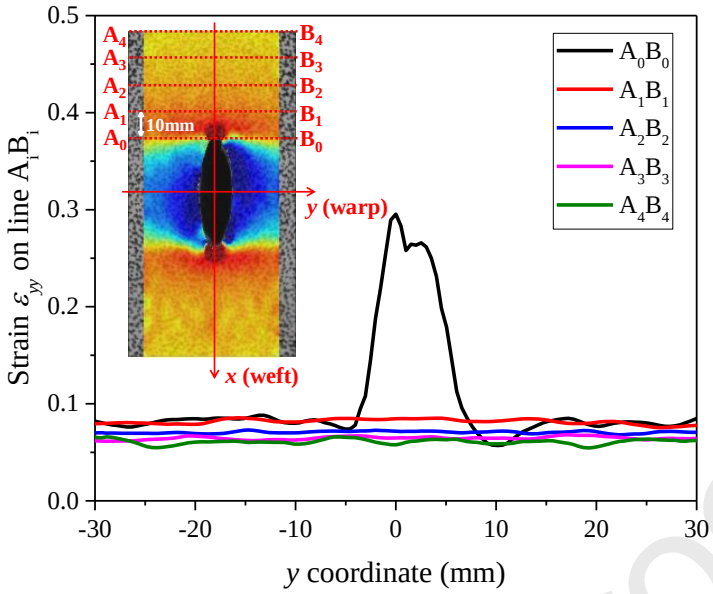

Fig. 16 Strain ε_{yy} at 100% σ_{max} on path A_iB_i (θ=90°, 2a=40 mm)

As shown in Fig. 15, although the maximum strain in the left side is smaller than the right side, the average strain is nearly equal. The inequality of the maximum strain may be consequence of the cutting procedure which could create slight defect at the crack tip.

From the strain distributions (Fig. 15), the increases in crack length can also be monitored. Since the zero strain part in the middle of the diagram represent the crack, it increases gradually with the increase of load. This is not caused by crack propagation (because no yarn rupture was observed), but results from the overall extension along the crack direction.

For different initial crack length, the average strain and the strain concentration factor (SCF) at 100% σ_{max} are summarized in Fig. 17. The average strain decreases with the increases of initial crack length, with similar trend for 0° and 90° crack, as also observed for TRS in Fig. 13. The average ε_{yy} strain for 0° crack (warp direction) is higher than that of 90° crack (weft direction), this is due the higher stiffness in the crack direction. Moreover, the SCF shows an increasing tendency, which corresponds also to the rise of the corresponding maximum strain

with the initial crack length.

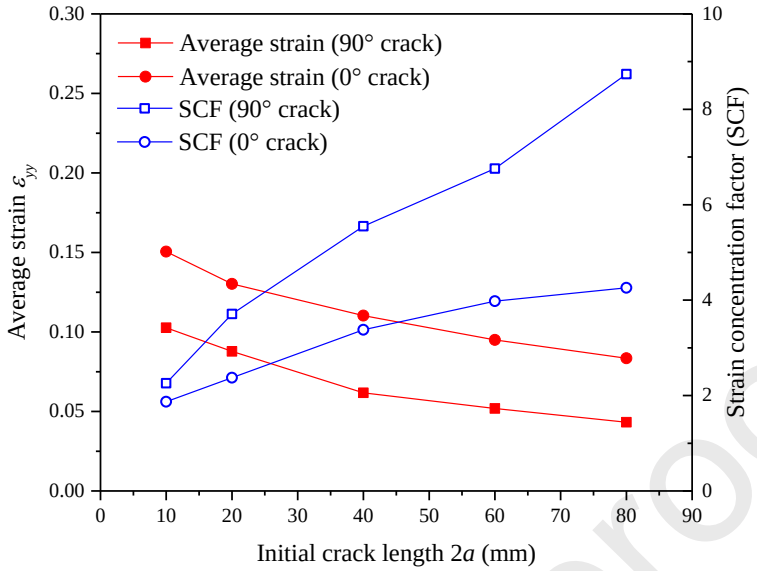

Fig. 17 Average strains and strain concentration factors (SCF)

As mentioned in Section 3.2, the maximum strain may be affected by DIC parameters, while the size of strain concentration zone is independent of the DIC parameters. Thus, the size of concentration zone is worthy for a quantitative comparison. Defining the strain concentration zone as the length along the path y=0, where the strain is larger than a certain multiple of the average strain, the size of strain concentration zone can be plotted. The length of the strain concentration zone is detailed in Fig. 18 for different multiple of the average strain. Fig. 18 highlights the considerable increase of the strain concentration zone with the initial crack length. In detail, the enlargement of the strain concentration zone for 90° crack is significantly higher than the 0° crack.

To sum up, the strain field characteristics of different initial crack lengths are collected in Table. 4.

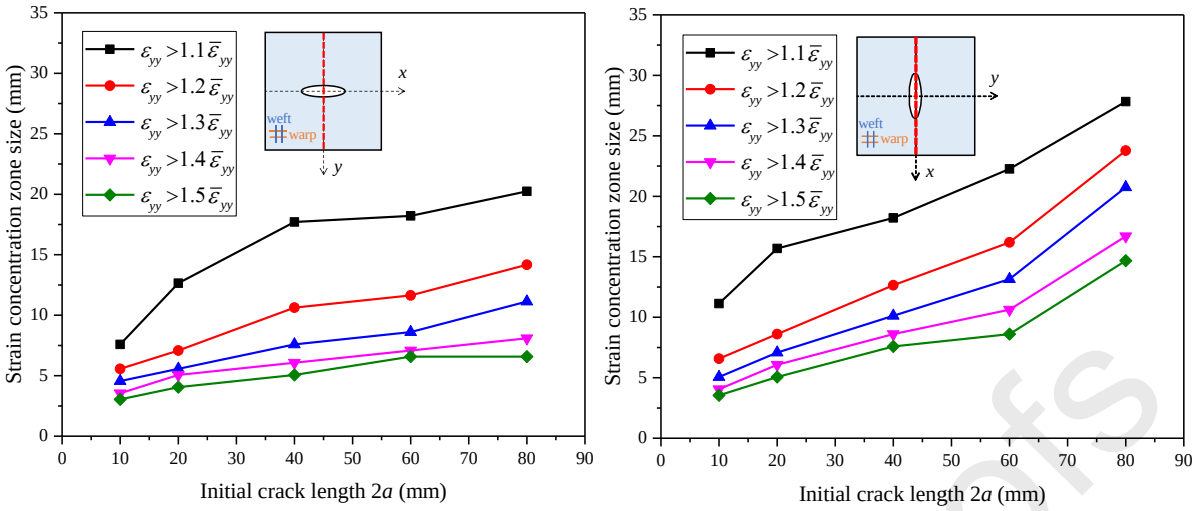

(a) 0° crack (b) 90° crack

Fig. 18 Strain concentration zone (SCZ) size

Table. 4 Strain field characteristics

2*a* (mm)	θ	Average strain	SCF	SCZ size (mm) $\varepsilon_{yy}>1.2\bar{\varepsilon}_{yy}$	SCZ size (mm) $\varepsilon_{yy}>1.5\bar{\varepsilon}_{yy}$
10	0°	0.1506	1.87	5.6	3.0
	90°	0.1026	2.26	6.6	3.5
20	0°	0.1302	2.37	7.1	4.0
	90°	0.0878	3.71	8.6	5.1
40	0°	0.1103	3.38	10.6	5.1
	90°	0.0617	5.55	12.7	7.6
60	0°	0.0950	3.98	11.6	6.6
	90°	0.0519	6.76	16.2	8.6
80	0°	0.0835	4.26	14.2	6.6
	90°	0.0432	8.74	23.8	14.7

5. Effect of initial crack orientation on biaxial tearing behaviors

5.1 Tearing stress-displacement curves and tearing process analysis

The nominal tearing stress-displacement curves for different crack orientations are given in Fig. 19. On one hand, varying the crack orientation, the curves show slight difference of the slope. On the other hand, the crack orientation has a certain influence on the tearing residual strength and the post-peak behavior. Unlike the 0° and 90° cracks, where the initial crack only affects the mechanical properties in its perpendicular direction, with the inclination of the crack, both warp and weft yarns are involved in the tearing process, thus the tearing residual strength is determined by the weakest direction. From the point of view of fracture mechanics, it is a mixed-mode fracture (in-plane tension and shear) for orthotropic material under biaxial tensile loading.

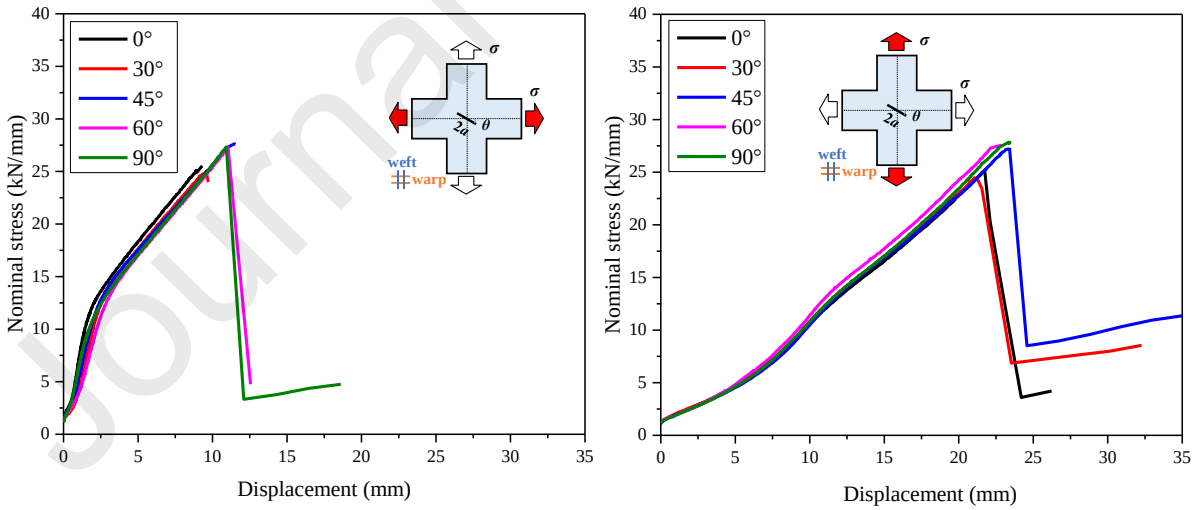

(a) Warp direction curves (b) Weft direction curves

Fig. 19 Stress-displacement curves of specimens with different initial crack orientation (2*a*=40 mm)

The tearing process of specimens with different initial crack orientation are given in Fig.

20. No obvious crack propagation was observed before complete failure, thus the tearing failures are brittle. Similar to 0° and 90° cracks, the initial crack opens gradually and changes from slit shape to spindle shape with the increase of load. However, the crack propagation paths in the final load step are very different. For 0°, 30° and 45° cases, the crack extends along 0° (warp) direction. For 60° and 90° cases, the crack extends along 90° (weft) direction. If we define the threshold crack angle as the initial crack angle for which the crack tends to propagate in both warp and weft direction at the same time, as for an isotropic material under 1:1 biaxial tensile load, the threshold crack angle must be 45°. For the PVC coated fabric tested herein, the tearing resistance is slightly higher in warp direction, hence the threshold crack angle is larger than 45°.

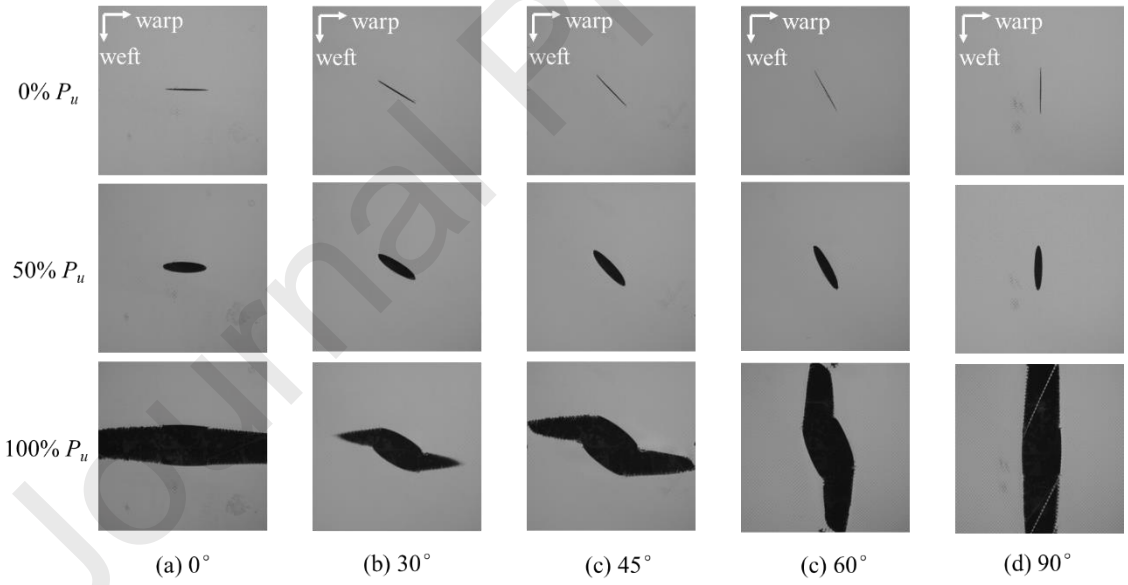

Fig. 20 Tearing process of specimens with different initial crack orientation (2a=40 mm), at different level of the ultimate load P_u.

Adopting the fracture toughness criterion [36], under the 1:1 biaxial tensile load, the threshold crack angle θ^*can be obtained by solving the following equation set:

$$\begin{cases} K_I^{weft} = Y(\rho)\cdot F(a/W)\cdot C_{11}(\theta^*)\cdot\sigma_c\sqrt{\pi a} = K_{IC}^{weft} \\ K_I^{warp} = Y(\rho)\cdot F(a/W)\cdot C_{11}(\frac{\pi}{2}-\theta^*)\cdot\sigma_c\sqrt{\pi a} = K_{IC}^{warp} \end{cases} \tag{7}$$

$$C_{11}(\alpha) = \frac{3}{4}\cos\frac{1}{2}\alpha + \frac{1}{4}\cos\frac{3}{2}\alpha \tag{8}$$

where $Y(\rho)$ is the orthotropic correction factor, $F(a/W)$ is the finite size correction factor, C_{11} is a coefficient related to the crack propagation orientation α given by Eq. (8) ([36]). The solution of Eq. (7) can be obtained by finding the zero point in Fig. 21, for $K_{IC}^{warp}/K_{IC}^{weft}$=1.00, 1.05, 1.10, 1.15 and 1.20. Therefore, the threshold crack angles θ^* are 45°, 47.3°, 49.4°, 51.5° and 53.4° respectively.

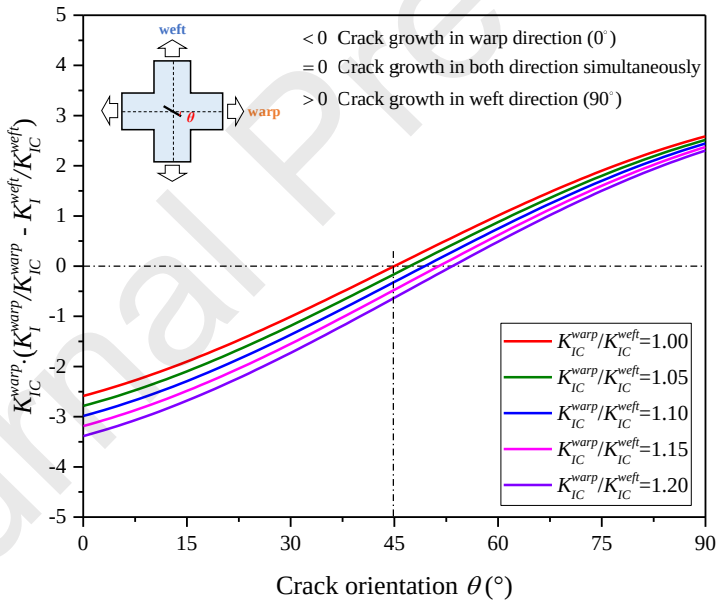

Fig. 21 Determination of threshold crack angle

5.2 Tearing residual strength

Tearing residual strengths σ_{res} of different crack orientations are illustrated in Fig. 22 and Table. 5. With the variation of crack orientation, the TRS has the maximum value 28.26 kN/m

for the crack orientation of 45°. It should be pointed out that it is not a general finding. Results in [15,16] shows that the TRS get its largest value at the crack orientation of 60°. It depends on the orthotropic properties of the tested fabrics.

Table. 5 Tearing residual strengths (average and standard deviation of three replicas) under different initial crack orientation (kN/m)

crack orientation θ	0° (warp)	30°	45°	60°	90° (weft)
Avg. TRS	25.87	25.37	28.26	26.50	27.01
S.D.	0.63	0.55	0.68	0.67	0.38

As mentioned in [7,15,16,37], the inclined crack can be simplified as 0° or 90° crack by projecting to an axis along the yarn direction (can be warp or weft direction, it depends on the crack growth direction). The crack length obtained from the projection is defined as the equivalent crack length. Combined with the observed crack growth direction shown in Fig. 20, the equivalent crack length is given in Table. 6. Obviously, the equivalent crack length is smaller than the initial crack length. Substituting these equivalent crack lengths into Eq. (3) and (4), the predicted TRS can be obtained. Unsurprisingly, the predicted TRS of inclined crack is larger than 0° or 90° crack, due to the smaller equivalent crack length. The prediction underestimates the TRS of inclined initial crack by about 10%. The error may be attributed to the omission of the shear stress effect.

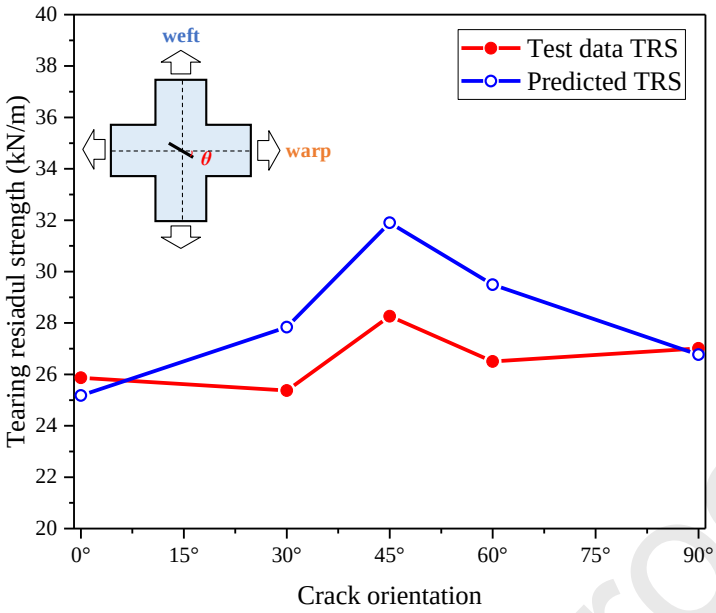

Fig. 22 TRS under different crack orientation (2a=40 mm)

Table. 6 Equivalent crack length and predicted TRS under different crack orientation

Initial crack orientation	Crack growth direction	Equivalent crack length (mm)	Predicted TRS (kN/m)	Experimental TRS (kN/m)	Relative difference (%)
0° (warp)	0° (warp)	40 (warp)	25.18	25.87	2.66
30°	0° (warp)	34.64 (warp)	27.84	25.37	9.77
45°	0° (warp)	28.28 (warp)	31.90	28.26	12.89
60°	90° (weft)	34.64 (weft)	29.49	26.50	11.28
90° (weft)	90° (weft)	40 (weft)	26.77	27.01	0.89

5.3 Strain field analysis

The full-field strain distribution of 45° crack obtained by DIC is shown in Fig. 23. The normal strain ε_{xx} (warp) and ε_{yy} (weft) maps in Fig. 23 (a) and (b) display positive strains for most part of ROI, while negative strain zone is close to crack tips. The main difference of the

two distributions is the average value, ε_{yy} (weft) is larger than ε_{xx} (warp), and this is because the higher stiffness in warp direction as shown in the stress-displacement curves (Fig. 19).

The shear strain component ε_{xy} maps in Fig. 23 (c) reveal non-uniform distribution in the whole ROI and exhibit perfect symmetry about the initial crack direction. On both side of the crack, there is a large triangular zone of positive shear strain, while at the tips of the crack the shear strain is mainly negative, which shows different rotation along the crack edge. This reveals the importance of the shear stress for the inclined crack configurations.

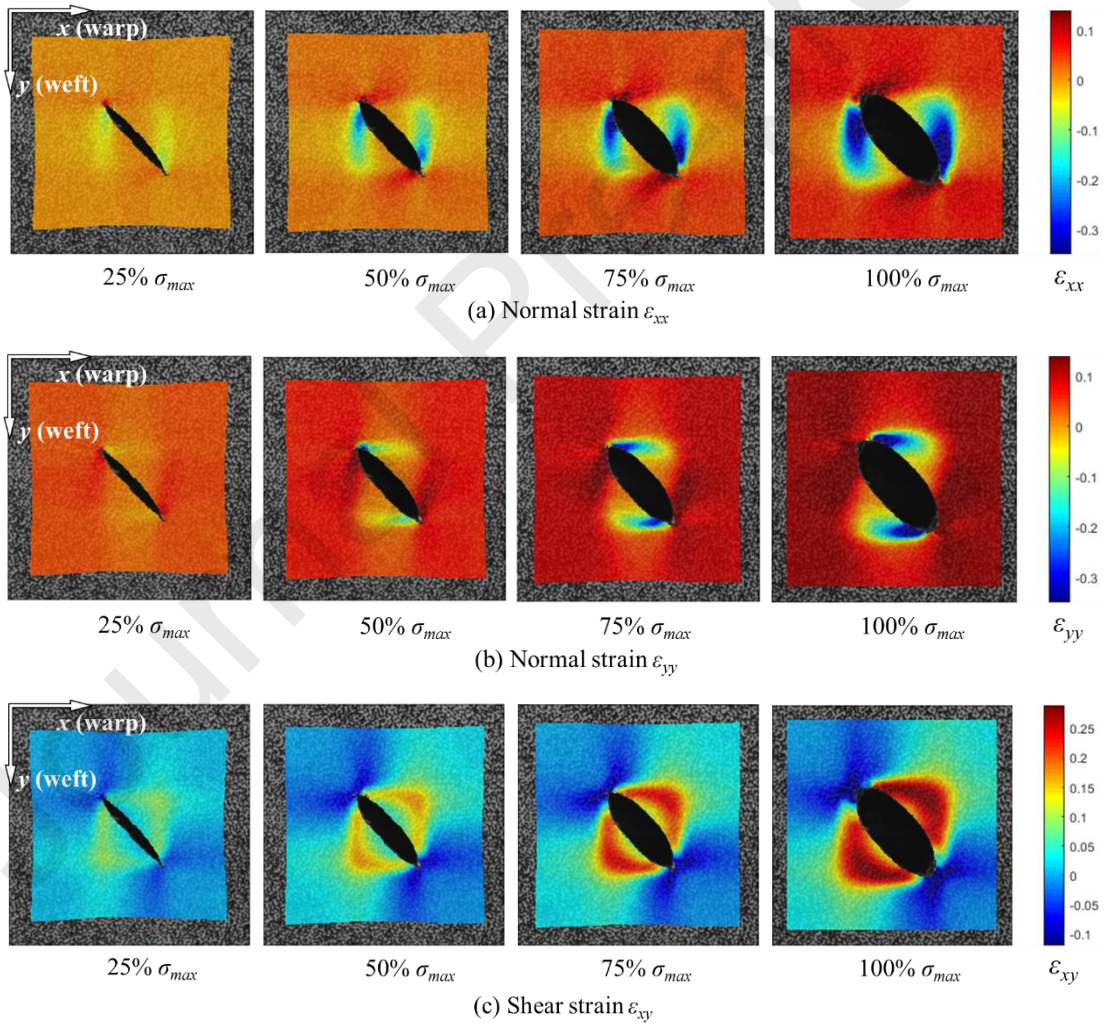

Fig. 23 Full-field strain under different load level, (θ=45°, 2a=40 mm,)

6. Conclusions

Central crack tearing tests under biaxial tensile loading were conducted for a polyester yarn textile fabric coated with polyvinylchloride. The experimental campaign intended to study the effect of initial crack length and orientation on tearing behavior, considering various aspects such as: the shape of stress-displacement curves, the tearing residual strength (TRS), the tearing process and the full field strain. The following conclusions can be drawn:

(1) With the increase of applied load, the initial crack opens gradually and changes from sharp slit to spindle shape, no obvious crack propagation was observed before complete failure. Regardless of the crack orientation, the final crack propagation always follows warp or weft direction. The threshold crack orientation θ^* can be analytically estimated, it depends on the loading ratio and fracture toughness in both direction. If the initial crack orientation is smaller than θ^*, crack propagates in warp direction. For the considered material, the threshold crack orientation lies between 45° and 60°.

(2) For 0° and 90° cracks, the strain component perpendicular to crack propagation direction plays an important role. It had a circular strain concentration zone at crack tip. Away from that, strain quickly becomes uniformly distributed. Along the crack propagation path, both the maximum strain and the average strain increase with the increase of external load, but the strain concentration factor decreases due to the crack opening and crack tip blunting. For inclined cracks, both the shear strain and the normal strain perpendicular to crack propagation direction play an important role.

(3) The TRS is greatly affected by the initial crack length. For fixed initial crack length, the TRS does not change significantly with the variation of crack orientation. The maximum TRS occurs for 45° crack. With the increase of initial crack length, the TRS decreases

nonlinearly and can be well fitted by a simple exponential function.

Declaration of Competing Interest

The authors declare that they have no known competing financial interests or personal relationships that could have appeared to influence the work reported in this paper.

Acknowledgements

The authors would like to acknowledge the National Natural Science Foundation of China (Grant No. 51678192) and the National Key Research and Development Project (Project No. ZDYF20190094) for the financial support. Prof. Wujun Chen and Ph.D. Chengjun Gao offered assistance in biaxial tensile tests. Mr. Liwei Zhu helped to cut the row material into cruciform specimens.

Data availability

The raw/processed data required to reproduce these findings cannot be shared at this time due to technical or time limitations.

Appendix A

The finite size correction factor $F(a/W)$ only accounts for the effect of geometry and boundary conditions on the stress intensity factor (SIF). Thus excluding the effect of material mechanical behavior, the calculation can be based on isotropic material model. For the

cruciform specimen shown in Fig. 1 (a), $F(a/W)$ can be calculated by [36]:

$$F(a/W)=\frac{K_I}{\sigma\sqrt{\pi a}} \tag{A-1}$$

Where K_I is the SIF of the cruciform specimen obtained by finite element analysis, and $\sigma\sqrt{\pi a}$ is the SIF of a cracked infinite body.

Finite element analyses were performed on Abaqus/standard 6.13, it provides a domain integral method to evaluate the SIF for any loading, and holds high accuracy with rather coarse mesh in two dimensions [38]. Half of the cruciform specimen was modeled due to the symmetry, boundary conditions of the finite element model and the mesh pattern near the crack tip are shown in Fig. A-1. Second-order plane stress elements CPS8 and CPS6 are adopted, the general mesh size outside the crack tip region is about 0.5mm. To calculate the SIF by contour integral method, ring-shaped mesh should be used surrounding the crack tip. In this model, a circular contour integral area with the radius of 3mm was adopted, it contains 10 layers of ring-shaped mesh, which is fine enough to obtain a mesh-independent result.

For a given specimen geometry and boundary conditions, $F(a/W)$ only relates to the a/W and it is independent of the elastic parameters and applied stress intensity [36]. Therefore, without loss of generality, an arbitrary given elastic modulus and Poisson's ratio, of intensity E = 8 GPa and ν = 0.3, were adopted. An arbitrary uniform tensile stress was applied, on the top and bottom boundary of the vertical arms and right boundary of the horizontal arm (Fig. A-1), of intensity σ=20 MPa.

Finally, the numerically predicted K_I, the calculated $\sigma\sqrt{\pi a}$, and thus $F(a/W)$ for different

crack size are listed in Table. A-1.

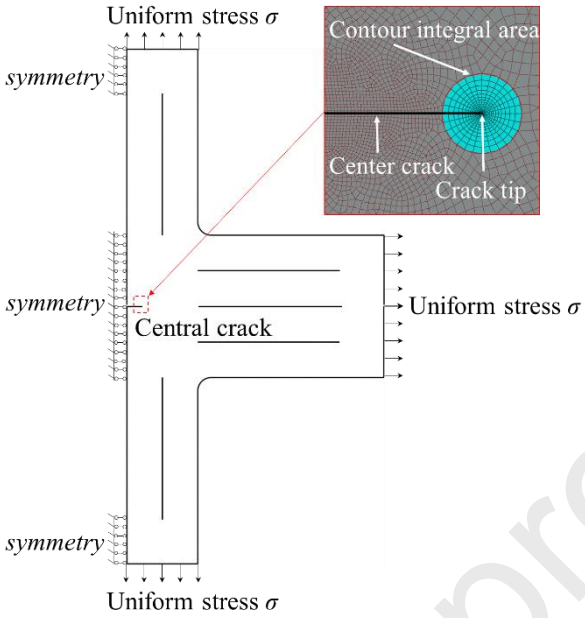

Fig. A-1 Sketch of half cruciform specimen and finite element mesh at the crack tip

Table. A-1 Estimated K_I and finite size correction factor of the cruciform specimen

$2a$ (mm)	K_I (N·mm$^{-3/2}$)	σ $\sqrt{\pi a}$ (N·mm$^{-3/2}$)	$F(a/W)$
10	75.53	79.267	0.953
20	107.8	112.100	0.962
40	158.3	158.533	0.999
60	205.6	194.163	1.059
80	256.9	224.200	1.146

References

[1] Hu J, Chen W, Qu Y, Yang D. Safety and serviceability of membrane buildings: A critical review on architectural, material and structural performance. Eng Struct. 2020;210:110292.

[2] He R, Sun X, Wu Y. Central crack tearing test and fracture parameter determination of PTFE coated fabric.

Constr Build Mater. 2019;208:472-81.

[3] Gao C, Chen W, Hu J, Zhao B. A new constitutive model on biaxial tensile behavior of architectural fabrics. Polym Test. 2020;87:106519.

[4] Carvelli V. Biaxial tensile properties of reinforcements in composites. Composite Reinforcements for Optimum Performance. 2nd Ed. Cambridge: Woodhead Publishing; 2020. 307-332.

[5] Ko WL. Fracture Behavior of a Nonlinear Woven Fabric Material. J. Compos Mater. 1975;9:361-9.

[6] Minami H. Strength of Coated Fabrics with Crack. Journal of Coated Fabrics. 1978(7):269-92.

[7] Bigaud D, Szostkiewicz C, Hamelin P. Tearing analysis for textile reinforced soft composites under mono-axial and bi-axial tensile stresses. Compos Struct. 2003;62(2):129-37.

[8] Maekawa S, Yoshino T. Tear Propagation of a High-Performance Airship Envelope Material. J. Aircraft. 2008;45(5):1546-53.

[9] Chen J, Chen W, Zhao B, Yao B. Mechanical responses and damage morphology of laminated fabrics with a central slit under uniaxial tension: A comparison between analytical and experimental results. Constr Build Mater. 2015;101:488-502.

[10] Zhang Y, Xu J, Zhou Y, Zhang Q, Wu F. Central tearing behaviors of PVC coated fabrics with initial notch. Compos Struct. 2019;208:618-33.

[11] Chen J, Chen W, Zhou H, Zhao B, Ding Y, Zhang N. Central tearing characteristics of laminated fabrics: Effect of slit parameter, off-axis angle, and loading speed. J Reinf Plast Comp. 2017:621085110.

[12] Szostkiewicz C, Hamelin P. Stiffness Identification and Tearing Analysis for Coated Membranes under Biaxial Loads. J Ind Text. 2000;30(2):128-45.

[13] Godfrey TA, Rossettos JN, Bosselman SE. The Onset of Tearing at Slits in Stressed Coated Plain Weave

Fabrics. J. Appl Mech-T. ASME. 2004;71:879-86.

[14] Luo Y, Hu H. Mechanical properties of PVC coated bi-axial warp knitted fabric with and without initial cracks under multi-axial tensile loads. Compos Struct. 2009;89(4):536-42.

[15] Chen J, Chen W. Central Crack Tearing Testing of Laminated Fabric Uretek3216LV under Uniaxial and Biaxial Static Tensile Loads. J Mater Civil Eng. 2016;28(7):4016028.

[16] Wang F, Chen Y, Liu G, Guo Z, Fu G. Experimental investigation and theoretical analysis of tear propagation of GQ-6 airship envelope. J Ind Text. 2016;48(1):304-21.

[17] Lomov SV, Boisse P, Deluycker E, Morestin F, Vanclooster K, Vandepitte D, et al. Full-field strain measurements in textile deformability studies. Compos Part A Appl Sci Manuf . 2008;39(8):1232-44.

[18] Jurjo DLBR, Magluta C, Roitman N, Batista Gonçalves P. Analysis of the structural behavior of a membrane using digital image processing. Mech Syst Signal Process . 2015;54-55:394-404.

[19] Hu J, Gao C, He S, Chen W, Li Y, Zhao B, et al. Effects of on-axis and off-axis tension on uniaxial mechanical properties of plain woven fabrics for inflated structures. Compos Struct. 2017;171:92-9.

[20] Shi T, Chen W, Gao C, Hu J, Zhao B, Wang P, et al. Biaxial constitutive relationship and strength criterion of composite fabric for airship structures. Compos Struct. 2019;214:379-89.

[21] Xu J, Zhang Y, Wu M, Zhao Y. A phenomenological material model for PTFE coated fabrics. Constr Build Mater. 2020;237:117667.

[22] Trejo EA, Ghazimoradi M, Butcher C, Montesano J. Assessing strain fields in unbalanced unidirectional non-crimp fabrics. Compos Part A Appl Sci Manuf. 2020;130:105758.

[23] Dinh TD, Rezaei A, Puystiens S, Van Craenenbroeck M, Carbonez K, De Laet L, et al. A study of tension fabric membrane structures under in-plane loading: Nonlinear finite element analysis and validation. Compos

Struct. 2015;128:10-20.

[24] Sun X, Wu H, Wu Y. Vibration monitoring of an open-type one-way tensioned membrane structure based on stereovision. Rev Sci Instrum. 2019;90(7):75112.

[25] Liu M, Guo J, Li Z, Hui C, Zehnder AT. Crack propagation in a PVA dual-crosslink hydrogel: Crack tip fields measured using digital image correlation. Mech Mater. 2019;138:103158.

[26] Liu M, Guo J, Hui CY, Zehnder AT. Application of Digital Image Correlation (DIC) to the Measurement of Strain Concentration of a PVA Dual-Crosslink Hydrogel Under Large Deformation. Exp Mech. 2019;59(7):1021-32.

[27] Membrane Structures Association of Japan, MSAJ/M-02-1995, Testing Method for Elastic Constants of Membrane Materials, 1995.

[28] Gao C, Chen W, Shi T, Hu J, Zhao B, Qiu Z. Response surface characterization for biaxial tensile properties of envelope fabrics under multiple stress ratios. Compos Struct. 2019;230:111482.

[29] Shi T, Chen W, Gao C, Hu J, Zhao B, Wang P, et al. Biaxial strength determination of woven fabric composite for airship structural envelope based on novel specimens. Compos Struct. 2018;184:1126-36.

[30] Blaber J, Adair B, Antoniou A. Ncorr: Open-Source 2D Digital Image Correlation Matlab Software. Exp Mech. 2015;55(6):1105-22.

[31] Ncorr v1.2 DIC Algorithms. http://www.ncorr.com/index.php/dic-algorithms

[32] International Digital Image Correlation Society. A Good Practices Guide for Digital Image Correlation. 2018.

[33] Sutton MA, Orteu J, Schreier HW. Image correlation for shape, motion and deformation measurements: basic concepts, theory and applications: Springer, 2009.

[34] Pan B, Xie H, Guo Z, Hua T. Full-field strain measurement using a two-dimensional Savitzky-Golay digital

differentiator in digital image correlation. Opt Eng. 2007;46(3):33601-336010.

[35] Harilal R, Ramji M. Adaptation of Open Source 2D DIC Software Ncorr for Solid Mechanics Applications.9th International Symposium on Advanced Science and Technology in Experimental Mechanics. 2014. http://ncorr.com/download/publications/harilalapplication.pdf

[36] Anderson TL. Fracture mechanics: fundamentals and applications. New York: CRC Press; 2017. Pages 51-54 & 85-86

[37] Bao H, Wu M, Zhang X. Tearing analysis of PVC coated fabric under uniaxial and biaxial central tearing tests. J Ind Text. 2020:2025636363.

[38] Abaqus 6.13 Benchmarks Manual. 1.16.1 Contour Integral Evaluation: Two-Dimensional Case.

[39] Hammouda, M., Fayed, A. & Sallam, H. Stress intensity factors of a central slant crack with frictional surfaces in plates with biaxial loading. Int J Fracture. 2004;129:141–148.

[40] Ali O. Ayhan, Three-dimensional mixed-mode stress intensity factors for cracks in functionally graded materials using enriched finite elements, Int J Solids Struct. 2009;46:796-810.